communications biology

A Nature Portfolio journal

Article

https://doi.org/10.1038/s42003-025-07741-5

The role of the glutathione pathway in tracheal regeneration with aortic allografts through antioxidant-driven tissue integration

Shixiong Wei[1,2,3,6], **Yao Zhi**[1,6], **Zhou Chen**[4,5], **Yiyuan Zhang**[1,2], **Kexing Duan**[1], **Mingqian Li**[1,6] & **Guoyue Lv**[1,6]

Tracheal regeneration remains a major challenge due to the lack of efficient graft integration and functional restoration. Current approaches fail to address oxidative stress-induced tissue remodeling. Here, we show that the glutathione pathway plays a pivotal role in tracheal regeneration with aortic allografts by modulating redox homeostasis and promoting host-graft integration. Through transcriptomic profiling, histological analyses, and functional assessment, we demonstrate that antioxidant-driven tissue remodeling enhances epithelialization, neovascularization, and extracellular matrix organization, thereby improving graft stability and biomechanical properties. These findings provide mechanistic insights into oxidative stress-mediated tissue remodeling and suggest that targeting redox signaling could optimize bioengineered tracheal grafts for clinical translation.

Tracheal reconstruction poses significant challenges in regenerative medicine due to the intricate structural and functional demands of tracheal tissues. The reconstruction of extensive tracheal defects arising from malignancies, prolonged intubation, congenital anomalies, and trauma often surpasses the capabilities of traditional surgical interventions. These conventional methods frequently result in complications such as stenosis and recurrent infections[1,2].

Recent advancements in tissue engineering have introduced aortic allografts as promising scaffolds for tracheal reconstruction. Their structural and biomechanical compatibility with the trachea offers a distinct advantage. However, the integration and functionality of these grafts are often compromised by oxidative stress associated with surgical trauma and ischemic conditions post-implantation[3]. The oxidative stress response significantly impacts cellular survival and differentiation, which are critical to the healing process and the long-term success of graft integration[4].

The glutathione pathway, a principal antioxidant system within cells, plays an essential role in defending against oxidative stress induced by reactive oxygen species (ROS). This pathway, involving key enzymes such as glutamate-cysteine ligase (GCLC), glutathione peroxidases (GPXs), glutathione reductase (GSR), and glutathione S-transferases (GSTs), is crucial for maintaining redox balance, thereby supporting tissue repair and regeneration[5]. The upregulation of these enzymes in models of tissue injury highlights their importance in post-surgical repair processes[6]. By integrating a comprehensive biochemical analysis with advanced imaging techniques, This study aims to investigate the involvement of the glutathione pathway in tracheal regeneration using aortic allografts, with a focus on understanding how antioxidant mechanisms influence tissue integration and cartilage regeneration[7,8].

Methods

Ethical statement

All animal experiments were approved by the Institutional Animal Care and Use Committee (IACUC) of The First Hospital of Jilin University. We have complied with all relevant ethical regulations for animal use[9].

Animal preparation and housing

Sixty 10-week-old male Sprague-Dawley rats, weighing ~250–300 g, were procured from Beijing Vital River Laboratory Animal Technology Co., Ltd. Twelve EGFP fluorescent SD rats were sourced from Cyagen Biosciences. The animals were divided into six postoperative time-point groups (1 day,

---

[1]Department of Hepatobiliary and Pancreatic Surgery, General Surgery Center, The First Hospital of Jilin University, 130021 Changchun, China. [2]Department of Thoracic Surgery, The First Hospital of Jilin University, 130021 Changchun, China. [3]Medicine & Engineering & Informatics Fusion and Transformation Key Laboratory of Luzhou City, 646000 Luzhou, China. [4]Institute of Atomic and Molecular Physics, Jilin University, 130012 Changchun, China. [5]Advanced Light Field and Modern Medical Treatment Science and Technology Innovation Center of Jilin Province, Jilin University, 130012 Changchun, China. [6]These authors contributed equally: Shixiong Wei, Yao Zhi, Mingqian Li, Guoyue Lv. ✉e-mail: lvgy@jlu.edu.cn

1 week, 1, 2, 3, and 6 months) for evaluation. Group sizes were: 1 day ($n = 6$), 1 week ($n = 6$), 1 month ($n = 8$), 2 months ($n = 8$), 3 months ($n = 8$), and 6 months ($n = 8$). An additional long-term follow-up group was assessed at 8 months ($n = 4$). The decision to use only male rats was based on the objective to eliminate the variability in results that may arise from hormonal fluctuations associated with the estrous cycles in females. Animals were acclimatized for one week before experimentation under controlled conditions (22 °C, 12-h light/dark cycle) with food and water available ad libitum.

Anesthesia and surgical procedure

Rats were anesthetized using an intraperitoneal injection of ketamine (90 mg/kg) and xylazine (10 mg/kg). Tracheal transplantation involved replacing a 1.0-cm segment of the cervical trachea, approximately 30–35% of the total tracheal length, with a silicone-stented aortic allograft. This segment size was chosen to closely replicate clinical tracheal reconstruction conditions while ensuring a viable airway post-operation.

Allografts, harvested from genetically similar donor rats, were prepared by removing any connective tissue and endothelial lining and then cutting to match the resected tracheal length. A silicone stent was inserted into the lumen to maintain structure during implantation and initial healing. Grafts were sterilized with ethylene oxide to ensure aseptic conditions. The surgical sites were sutured using 6-0 absorbable sutures (Ethicon, Vicryl). For the proximal anastomosis, the animals were transitioned from ventilator support to spontaneous breathing under anesthesia. Spontaneous ventilation was maintained through the distal trachea while performing the proximal graft-to-trachea anastomosis. The postoperative care included administering buprenorphine (0.05 mg/kg subcutaneously) every 12 h for 48 h for pain management.

Silicone stent removal was performed through a second cervical surgery beginning at 3 months postoperatively. Not all animals underwent stent removal, as some were retained for evaluating the effects of stent duration on graft structure and cartilage ring regeneration. The stent, which extended beyond the anastomoses by approximately two cartilage rings, was removed via an incision at the proximal airway near the pharyngeal region.

Tissue harvesting and histological analysis

Animals were euthanized at predefined intervals (1 day, 1 week, 1, 2, 3, and 6 months) using CO_2 inhalation and cervical dislocation. At each time point, enzymatic activity assays were performed on harvested samples to evaluate the activity of key enzymes in the glutathione pathway. Tissue samples were processed immediately after collection to ensure the preservation of enzymatic activity for accurate results. A subset ($n = 4$) was also assessed at 8 months post-operation to evaluate long-term graft integration and stability. Harvested tracheal grafts were fixed in 4% paraformaldehyde, embedded in paraffin, sectioned at 5 µm, and stained with Hematoxylin and Eosin (H&E) for general histology, and Toluidine Blue for cartilage analysis.

Graft integration was further evaluated macroscopically by observing the anastomotic sites for vascularization, tissue continuity, and the absence of lumen collapse or stenosis. Microscopically, Masson's trichrome staining was performed to assess connective tissue formation, while H&E staining was used to evaluate the interface between the graft and host tissue, as well as the inflammatory response.

Cellular recovery was assessed using immunohistochemical staining for key markers. Cytokeratin staining was employed to evaluate epithelial regeneration, while vimentin staining was used to examine mesenchymal recovery. Additionally, Ki-67 staining was performed to detect proliferative activity in the graft, providing insight into cellular repopulation and regenerative processes.

Immunohistochemistry and advanced imaging techniques

Tissue sections underwent immunohistochemical staining using primary antibodies (CD68, F4/80, Ki67, PCNA, CD31, VEGFR2, CK-18, α-Tubulin, Mucin5AC, Aggrecan, COL2; Abcam, 1:200 dilution) and fluorescent secondary antibodies (Alexa Fluor series, Invitrogen) for visualization. The luminal surface of the tracheal grafts was analyzed using SEM (JEOL JSM-6610LV) at 4, 6, and 8 months post-transplantation. Samples were fixed in glutaraldehyde, dehydrated through a graded ethanol series, dried, and coated with gold before imaging. Confocal microscopy (Leica SP8), scanning electron microscopy (SEM, JEOL JSM-6610LV), transmission electron microscopy (TEM, JEM-1400 Flash), and atomic force microscopy (AFM, Bruker Dimension Icon) were employed to analyze the grafts' surface and ultrastructure.

Stem cell visualization and quantification

Bone marrow-derived mesenchymal stem cells (MSCs) from EGFP fluorescent rats were used due to their stable and strong fluorescence, which allowed easy identification and tracking in tissue sections using fluorescent microscopy. The fluorescence signal from EGFP-positive cells remained detectable over the entire observation period, enabling longitudinal analysis of their localization and distribution. To confirm the functional identity of these cells, immunofluorescent staining with specific markers such as CK5 and CK14 was performed in conjunction with EGFP fluorescence visualization.

To track the homing and integration of EGFP-tagged MSCs, fluorescence imaging was performed at multiple time points post-transplantation (2 weeks, 1, 2, 3, and 6 months). EGFP-positive cells were identified using confocal microscopy to determine their localization within the graft, particularly in relation to the graft center, periphery, and anastomotic junctions. The intensity and spatial distribution of fluorescence were assessed to quantify the contribution of MSCs to tissue regeneration.

Bioinformatics and statistical analysis of imported single-cell RNA-seq data

We analyzed single-cell RNA sequencing data provided by an international collaborator to uncover key signaling pathways involved in tracheal regeneration. Using the Seurat package in R, we performed quality control, normalization, and feature selection. We then conducted differential gene expression analysis, pathway enrichment analysis, and trajectory inference with Monocle 3 to investigate cellular dynamics and signaling pathway activations critical for regeneration.

Verification of signaling pathways and molecular activation experiments

Following bioinformatics analysis, key components of the identified pathways were validated via quantitative polymerase chain reaction (PCR) and Western blotting. Based on these results, specific molecular agonists were administered to a new cohort of animals. The effects of this treatment on tracheal regeneration were assessed using a comprehensive suite of histological and imaging techniques.

To further validate the role of key glutathione pathway enzymes in tracheal regeneration, receiver operating characteristic (ROC) curve analysis was performed based on the densitometric quantification of Western blot results. This analysis was conducted to evaluate the diagnostic potential of these enzymes in distinguishing effective graft integration phases (1-, 2-, and 6-month postoperative samples marked as positive) from other phases (aorta, 1-day, 1-week postoperative samples, and trachea marked as negative). The ROC curves were generated for each enzyme individually, and a combined analysis using a multivariable logistic regression model was performed to assess the overall predictive value of these markers. Area under the curve (AUC) values were calculated to quantify the performance of each enzyme and the combined model.

Statistics and reproducibility

Statistical approaches were customized for the study's complex design and longitudinal data. Normality was verified using the Shapiro–Wilk test to justify the use of parametric tests. Linear mixed-effects models were applied to manage random effects from biological variability across subjects and repeated measurements, incorporating fixed effects (treatment, time, and their interaction) and random effects (individual variability). The significance of fixed effects was evaluated using Type III tests with Satterthwaite's approximation for degrees of freedom, and multiple testing adjustments were made with Tukey's honestly significant difference test. For bioinformatics analysis, data normalization was conducted using the Trimmed Mean of *M*-values method in edgeR, and pathway analyses were performed with Fisher's exact test. Statistical significance was set at a *p*-value threshold of <0.05, using SPSS version 25.0 and R version 4.0.3 for all analyses.

Reproducibility was ensured by conducting all experiments with at least three independent biological replicates, with each replicate representing an independent sample from a separate animal or experimental batch. For histological and molecular analyses, data were derived from multiple tissue sections per sample to account for intra-sample variability. Technical replicates were included where applicable, ensuring consistency across measurements. Details on sample sizes and specific numbers of replicates for each experiment are provided in the corresponding figure legends. All experiments were performed following standardized protocols to minimize variability, and independent validation was conducted for key findings using alternative methods where feasible.

GCLC activation assay using α-lipoic acid

To evaluate the effect of enhancing glutathione pathway activity on tissue regeneration, an experimental regimen using α-lipoic acid, a known activator of GCLC (the rate-limiting enzyme of glutathione synthesis), was administered to a subset of animals. α-Lipoic acid was prepared as a sterile solution and administered intraperitoneally at a dose of 50 mg/kg/day for the first-week post-transplantation. This was followed by a reduced maintenance dose of 25 mg/kg, administered three times weekly until the third month. This dosing regimen was selected based on prior studies demonstrating effective GCLC activation and antioxidant enhancement under oxidative stress conditions.

Control animals received equivalent volumes of saline injections to account for the procedural effects. Animals in both the treatment and control groups were monitored longitudinally, and grafts were harvested at 1, 2, and 3 months post-treatment for comparative analysis of histological, enzymatic, and molecular outcomes. Key outcomes included the evaluation of glutathione pathway enzyme expression, cartilage ring formation, epithelial regeneration, and vascularization, which were assessed using PCR, Western blotting, and advanced imaging techniques as described earlier.

Reporting summary

Further information on research design is available in the Nature Portfolio Reporting Summary linked to this article.

Results

Surgical outcomes

All surgical interventions were performed meticulously, with no perioperative fatalities. However, two rats developed severe respiratory distress due to granulomatous tissue formation at the anastomotic sites. These cases were observed at one month (Fig. 1Ba) and 1.5 months (Fig. 1Bb) post-surgery and both animals were euthanized as a result. Histological analysis confirmed that the obstruction was primarily due to excessive granulation tissue and inflammatory cell infiltration. These findings underline the challenges associated with graft integration and highlight the risk of airway obstruction during the early postoperative phase. For the remaining animals, longitudinal assessments showed progressive graft integration and functional recovery. By 3 months (Fig. 1Ac) and 6 months (Fig. 1Ad), the aortic allografts displayed significant structural stability with well-formed cartilage islands. Airway patency was maintained, and only mild narrowing of the lumen was observed, which did not impair respiratory function. By 8 months, the grafts exhibited near-complete structural restoration, with smooth integration at the graft–host junction and no discernible boundary between the graft and native tracheal tissue. While these structural features suggest functional compatibility, direct functional assessments, such as airflow studies, were not conducted in this study (Fig. 1Ae).

These observations were supported by macroscopic evaluations of the anastomotic sites, which showed smooth tissue continuity, robust vascularization, and the absence of significant complications in the majority of animals. The progression from early inflammatory responses to advanced tissue integration and regeneration highlights the long-term potential of aortic allografts for tracheal reconstruction.

Longitudinal graft assessment

Three and 6-month follow-ups showed significant graft integration and cartilage development. By three months, silicone stents maintained airway patency, with emerging cartilage islands that formed structured rings by 6 months. The grafts were structurally stable after stent removal, showing only mild airway narrowing that did not affect respiratory function. Rats breathed independently, with no respiratory distress observed (Fig. 1Ac, Ad). By eight months, the grafts resembled native tracheal tissue with no visible demarcation at the anastomotic sites, demonstrating sustained structural and functional restoration (Fig. 1Ae).

Histological insights

Histopathological analysis through HE staining revealed an evolution from granulomatous blockage to well-vascularized graft tissue with emerging submucosal glands and cartilaginous structures within the first 1.5 months post-surgery (Fig. 1Ba–d). By 6 months, the grafts exhibited mature epithelial linings and continuous cartilage indicative of advanced regenerative processes (Fig. 1Be, f). Toluidine Blue staining highlighted the progressive maturation of cartilage from scattered islands to structured rings, underscoring the grafts' adaptation and endogenous tissue-like properties (Fig. 1Bg, h).

Immunohistochemical findings

Immunostaining for CD68 and F4/80 was used to assess the early inflammatory response, specifically focusing on macrophage presence within the grafts. CD68 staining revealed a marked influx of macrophages during the first-week post-transplantation, with a noticeable reduction by the end of the first month (Fig. 1Ca, b). The F4/80 staining results corroborated these observations, indicating a similar pattern of macrophage activity over time (Fig. 1Ca, b).

Immunostaining for Ki67 and PCNA was used to examine cell proliferation within the grafts. Ki67 staining showed a peak in cellular proliferation during the first two weeks after surgery, while PCNA staining indicated elevated levels of cell replication throughout the first-month post-operation (Fig. 1Cc, d).

CD31 and VEGFR2 staining were used to track the development of blood vessels in the graft. Vascularization was first detected one month post-transplantation, with evidence of a well-developed microvasculature by three months (Fig. 1Ce, f).

Aggrecan and COL2 immunostaining were used to assess cartilage formation within the graft. At one month post-operation, isolated cartilage islands were observed, which progressed into more continuous and structured cartilage by six months (Fig. 1Cg, h). Additionally, α-tubulin and Mucin5AC staining showed the development and maturation of the respiratory epithelium and submucosal glands over time (Fig. 1Ci, j). CK18 staining was performed to evaluate the epithelial differentiation and structural organization of the respiratory epithelium within the graft. Positive CK18 signals were evident at three months post-transplantation, demonstrating well-organized epithelial cell layers indicative of functional epithelial regeneration (Fig. 1Ck). This finding correlates with the presence of mature epithelial structures observed in histological and microscopic analyses.

Advanced microscopic analysis

SEM was utilized to analyze the luminal surface morphology of tracheal grafts at four, six, and eight months post-transplantation. At 4 months post-transplantation, SEM images revealed sparse and disorganized ciliated epithelial cells on the luminal surface, marking the early stages of

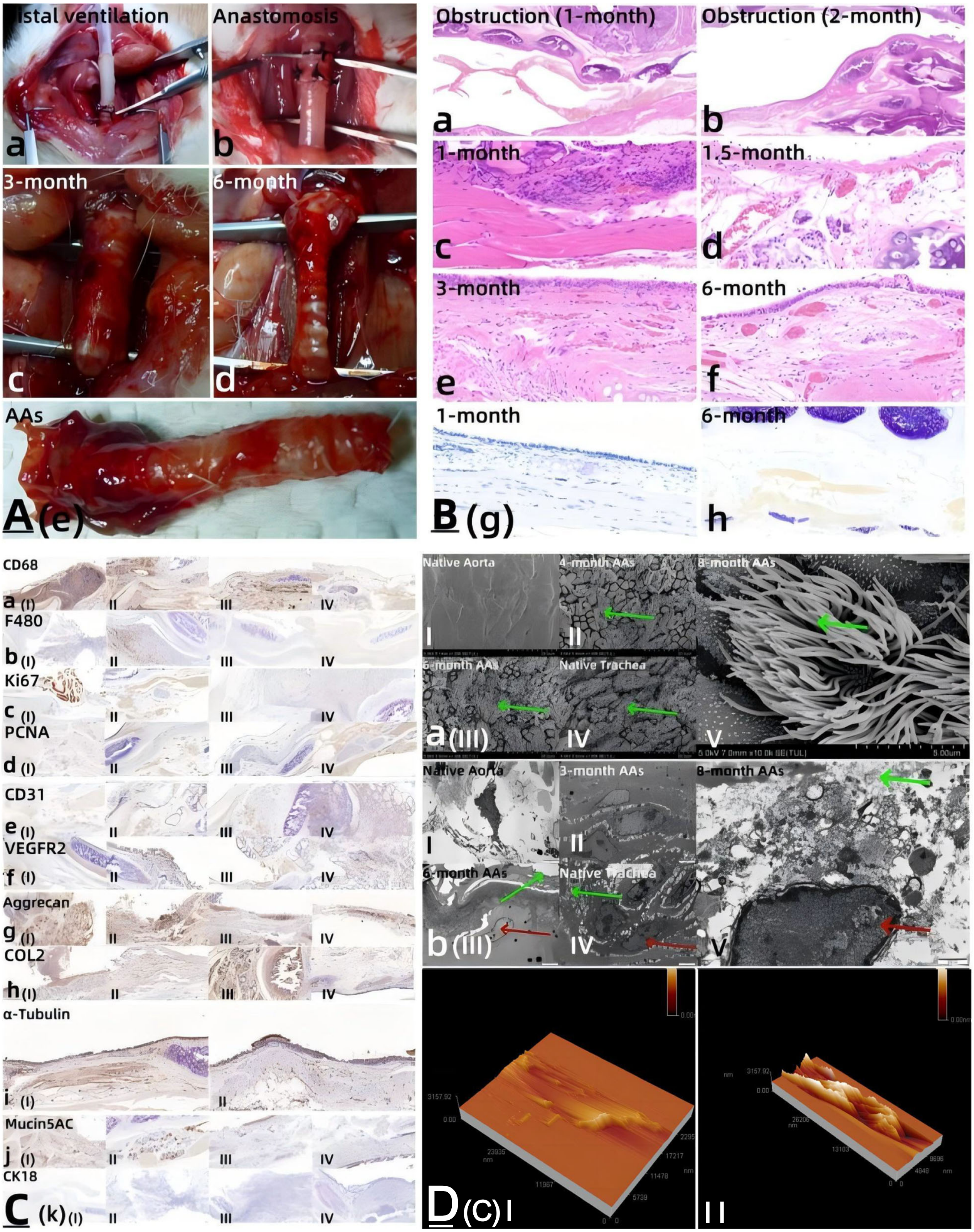

epithelial regeneration. By 6 months, the ciliated structures were more defined and continuous, reflecting the progression of epithelial maturation. By 8 months, SEM demonstrated a dense and uniform ciliated epithelial lining that closely resembled native tracheal tissue, indicating complete epithelial regeneration and the functional restoration of the graft.

TEM assessments at 3, 6, and 8 months post-implantation showed progressive ultrastructural integration. Early development of ciliated cells and goblet cells was noted at 3 months, with a disorganized epithelial structure. By 6 months, the features of a mature airway epithelium were visible, and by 8 months, full morphological and functional integration was confirmed.

Fig. 1 | Tracheal graft integration and histological evolution. **A** Longitudinal assessment of tracheal grafts showing integration and cartilage development over eight months. **Ac** and **Ad** illustrate progressive structural and functional restoration, with minimal airway narrowing as the grafts mature. **B** Histological analysis of tracheal grafts over time. Initially, the grafts exhibited granulomatous blockage **Ba, b**, which later resolved into well-vascularized tissue with emerging cartilage (**Bc**, **d**). Staining techniques used include Hematoxylin and Eosin (H&E) for general tissue structure and Toluidine Blue for cartilage visualization. **C** Immunohistochemical staining to assess early inflammatory response and cellular proliferation. **Ca, b** show CD68 and F4/80 staining to track macrophage infiltration from the anastomotic regions of the tracheal graft, while (**Cc, d**) show Ki67 and PCNA staining to highlight cell proliferation in the early postoperative period. 1 Da: SEM images of the luminal surface of tracheal grafts at 4, 6, and 8 months post-transplantation, showing the progressive regeneration of ciliated epithelial cells. Sparse and disorganized ciliated cells were observed at 4 months, defined and continuous structures at 6 months, and a dense, uniform ciliated epithelial lining resembling native tracheal tissue at 8 months (Green arrow: ciliated epithelium). **Db** TEM images taken at 3, 6, and 8 months highlight the structural development of key airway components. Early stages (3 months) show immature epithelial structures, while by eight months, the ultrastructure resembled a fully integrated native trachea, including the presence of well-organized ciliated cells and goblet cells (Green arrow: ciliated cell, Red arrow: goblet cell). **Dc** AFM provides high-resolution topographical mapping of the luminal surface. By 6 months, the surface texture showed fully formed epithelial structures, including fine details of mature cilia. At 8 months, AFM confirmed the structural stability of the graft with mature epithelial features closely resembling native tracheal tissue. **E** Vascular and cartilaginous development visualized through immunostaining. CD31 and VEGFR2 staining **Ce, f** show neovascularization beginning at one month and maturing by 6 months. Aggrecan and COL2 staining **Cg, h** illustrate the progressive maturation of cartilaginous tissue from isolated islands to a continuous framework by six months post-transplantation.

AFM provided detailed topographical mapping of the graft's luminal surface at 6 and 8 months. By 6 months, the surface displayed finely textured, mature cilia, indicative of developed epithelial structures essential for airway function. At 8 months, the epithelial surface was stable and fully integrated, closely mimicking native tracheal tissue.

Detailed immunofluorescent analysis and quantification of stem cell dynamics

Immunofluorescence staining using CK5, CK14, and DAPI monitored stem cell dynamics within the grafts, derived from the bone marrow of EGFP fluorescent Sprague-Dawley rats. In addition, Ki67 and PCNA staining were used to evaluate the proliferative state of EGFP-positive cells. Cells co-expressing these markers were considered activated and engaged in regenerative processes. Quantitative analysis showed two weeks post-transplantation, a modest number of activated stem cells were primarily located at the graft periphery, indicating early involvement in integration (Fig. 2Aa II). By one month, stem cell numbers significantly increased and were distributed more evenly across the graft (Fig. 2Aa III).

Using ImageJ software for objective quantification, a notable peak in stem cell populations occurred one-month post-transplantation, aligning with new cartilage and epithelial formation (Fig. 2Ab). Elevated stem cell levels persisted through two and three months, supporting ongoing tissue remodeling and maturation. Factors influencing stem cell migration and integration included the surgical microenvironment and local cytokines and growth factors.

EGFP fluorescence tracking to elucidate cellular contributions in regeneration

The application of EGFP-tagged cells provided crucial insights into the cellular dynamics within the grafts. Initially, intense fluorescence within the graft indicated a significant contribution from donor-derived cells. Over time, this fluorescence intensity decreased and was primarily observed migrating towards the anastomotic junctions (Fig. 2Ba I–V): Figure 2Ba I–V illustrates the sequential phases of EGFP-positive MSC localization and distribution within the aortic graft over time. At 2 weeks (I), EGFP-positive cells were predominantly concentrated near the graft periphery, reflecting an initial homing response. By one month (II), these cells showed increased presence within the central regions of the graft, suggesting active participation in tissue remodeling. At two months (III), a more uniform distribution was observed, indicating progressive integration of MSCs across the graft. By three months (IV), EGFP-positive cells localized predominantly at the anastomotic junctions, coinciding with regions of active vascularization. At six months (V), fluorescence intensity decreased overall, reflecting diminished MSC activity as tissue regeneration reached a more stabilized phase. This progression highlights the dynamic contribution of MSCs to different stages of graft integration and repair.

Role and integration of EGFP-tagged MSCs in tissue regeneration

The strategic injection of EGFP-tagged mesenchymal stem cells (MSCs) into the graft sites offered a unique perspective on their role in tissue regeneration. Figure 2Ca shows the inverted fluorescence microscopy image of EGFP-tagged MSCs cultured and expanded in vitro. The robust fluorescence signal and morphological uniformity of the cells confirm their readiness for subsequent transplantation. Post-transplantation, fluorescence imaging tracked the dynamic localization and distribution of EGFP-positive MSCs over time, as described in Panel 2B. Early imaging post-transplantation showed these cells initially localizing within the graft, with their fluorescence clearly observable. This fluorescence gradually decreased over time, with notable concentration at the graft's periphery by 3–6 months post-operation (Fig. 2Cb I–VI). The pattern of fluorescence reduction and peripheral concentration was consistent with the MSCs' involvement in critical regenerative activities such as new tissue formation and vascular development.

Bioinformatics analysis of tracheal regeneration

Single-cell RNA sequencing (scRNA-seq) was conducted to analyze the cellular composition within the grafts at various time points post-transplantation. The uniform manifold approximation and projection (UMAP) plot in Fig. 3A shows distinct cellular clusters across the experimental groups, including endothelial cells, epithelial cells, fibroblasts, lymph endothelial cells, macrophages, nerve cells, perichondrial cells, smooth muscle cells, and T cells. These cellular populations demonstrate the heterogeneity of the graft microenvironment and highlight the active involvement of multiple cell types in tissue remodeling and regeneration.

Figure 3Bb provides a more granular view of cell types in partially decellularized tracheal grafts (PDTG) at 1 month and 2 weeks, as well as syngeneic grafts at equivalent time points. The distribution of cell types among these groups is shown in the bar chart (Fig. 3Ba), which emphasizes the dynamic shift in cellular composition over time, with increasing contributions from epithelial and stromal cells in PDTGs.

Batch correction was performed to eliminate technical variability and ensure consistency across datasets. As shown in Fig. 3Cc, the UMAP plot before correction (Fig. 3C) illustrates distinct clustering biases, while the corrected data (Fig. 3Ca) demonstrates improved alignment of cellular clusters, ensuring reliable identification of cellular subtypes and pathways.

Using Monocle 3, we reconstructed the differentiation trajectories of progenitor cells and their progression toward specialized lineages such as chondrogenic cells. Figure 3Da depicts the pseudotime trajectory of progenitor cells, with branches corresponding to differentiated cell types integral to cartilage and epithelial regeneration. This analysis reveals the activation of key regenerative pathways and highlights the plasticity of progenitor cells within the graft.

Pathway enrichment analysis, detailed in Fig. 3E, identifies glutathione metabolism as a highly activated pathway in regenerating tissues. The figure

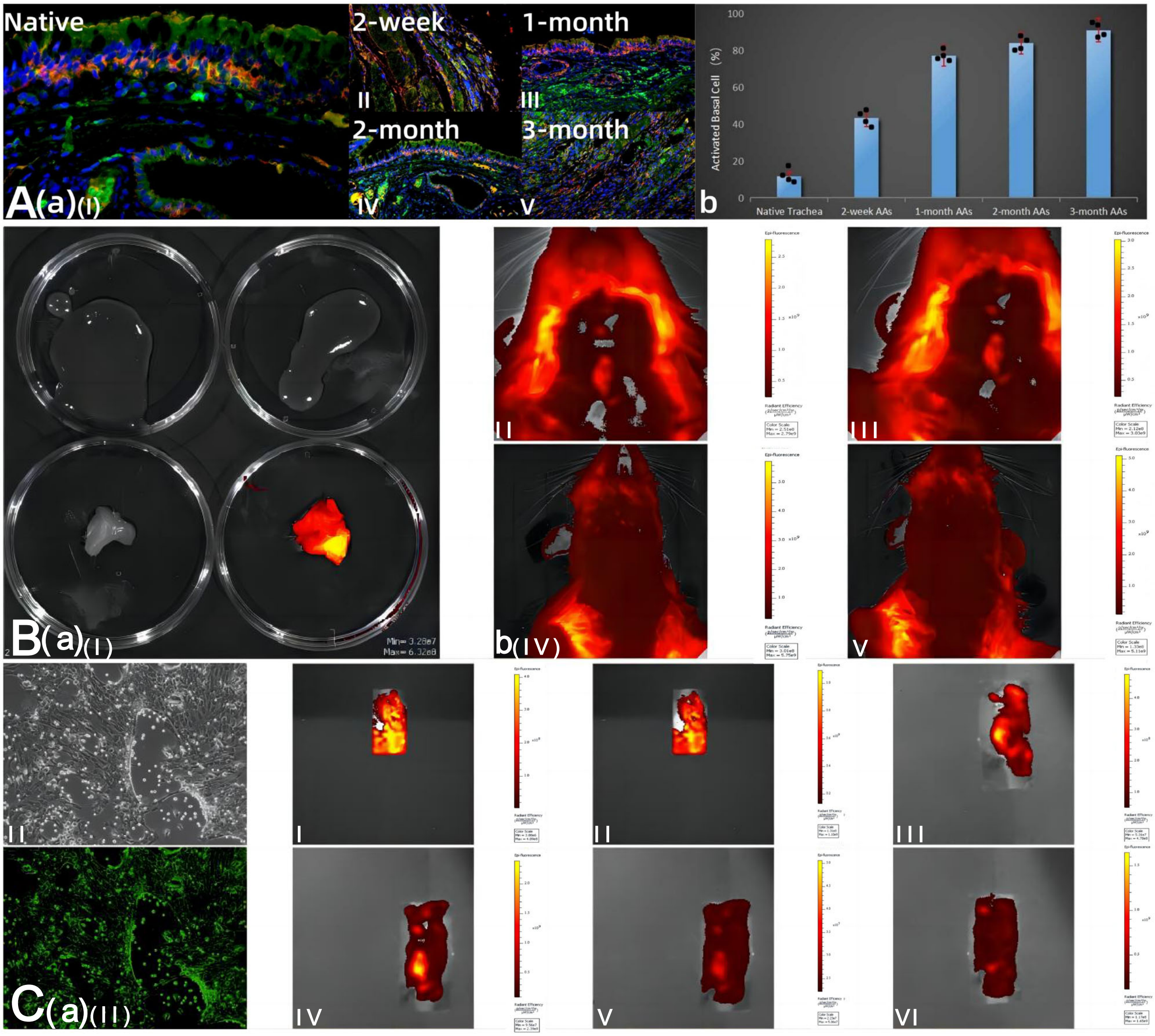

Fig. 2 | Stem cell dynamics and EGFP tracking. **A** Immunofluorescent analysis of stem cell distribution and activation within the grafts over time, using CK5, CK14, and DAPI staining. Images capture the increase and spatial distribution of stem cells from 2 weeks to 3 months post-transplantation (**Aa-IV**). **B** Sequential fluorescence imaging of EGFP-tagged MSCs in the aortic allografts (AAs) at 2 weeks (**I**), 1 month (**II**), 2 months (**III**), 3 months (**IV**), and 6 months (**V**). The images show the dynamic localization of MSCs, from an initial concentration near the graft periphery (**I**), to broader distribution within the graft center (**II**), and eventual migration towards the anastomotic junctions (**IV**). By six months (**V**), fluorescence intensity decreased, reflecting reduced MSC activity as regeneration stabilized (scale bar = 100 μm). **Ca** Inverted fluorescence microscopy image of EGFP-tagged mesenchymal stem cells (MSCs) cultured and expanded in vitro before transplantation. This panel demonstrates the robust fluorescence signal and uniformity of the expanded MSC population, confirming their suitability for in vivo tracking; **Cb I–VI**: Sequential imaging showing EGFP-positive MSCs over time. (**I**) Initial distribution of MSCs at the graft periphery at 2 weeks. (**II**) Broader localization by 1 month. (**III**) Increasing presence at the graft center by 2 months. (**IV**) MSC migration towards anastomotic regions at 3 months. (**V**) Integration and stabilization at 6 months. (**VI**) Reduction in fluorescence intensity as regeneration stabilizes by the later phase.

highlights the upregulation of genes associated with oxidative stress regulation and tissue repair, marked by red circles to emphasize the glutathione pathway. This pathway's activation correlates with enhanced enzymatic activity observed in earlier biochemical analyses, suggesting its pivotal role in mitigating oxidative stress during graft integration.

Validation of the glutathione pathway in tissue regeneration

PCR quantified the transcriptional activity of glutathione pathway enzymes—GCLC, GPXs, GSR, and GSTs—at various postoperative intervals (1 day, 1 week, 1, 2, and 6 months), with a significant peak at one month, indicating a robust enzymatic response during tissue remodeling (Fig. 4Aa–d). Comparative analysis against baseline native tissue samples demonstrated marked mRNA level increases.

Western blot analysis assessed the protein expression of these enzymes at the same intervals, confirming elevated levels in grafts compared to native tissues, peaking at one-month post-operation (Fig. 4B). Densitometric analysis of the Western blots, normalized to β-actin, validated these findings, showing a sustained elevation in enzyme levels indicative of ongoing oxidative stress management and tissue stabilization.

ROC curve analysis was conducted to evaluate the predictive significance of the glutathione pathway enzymes in tracheal regeneration. GCLC, GPXs, GSR, and GSTs exhibited AUC values of 0.787, 0.806, 0.787, and 0.806, respectively, indicating strong discriminatory power for identifying effective graft integration. The combined analysis using all four enzymes resulted in an AUC of 0.796, highlighting their synergistic role in predicting successful tissue integration (Fig. 4C). These findings reinforce

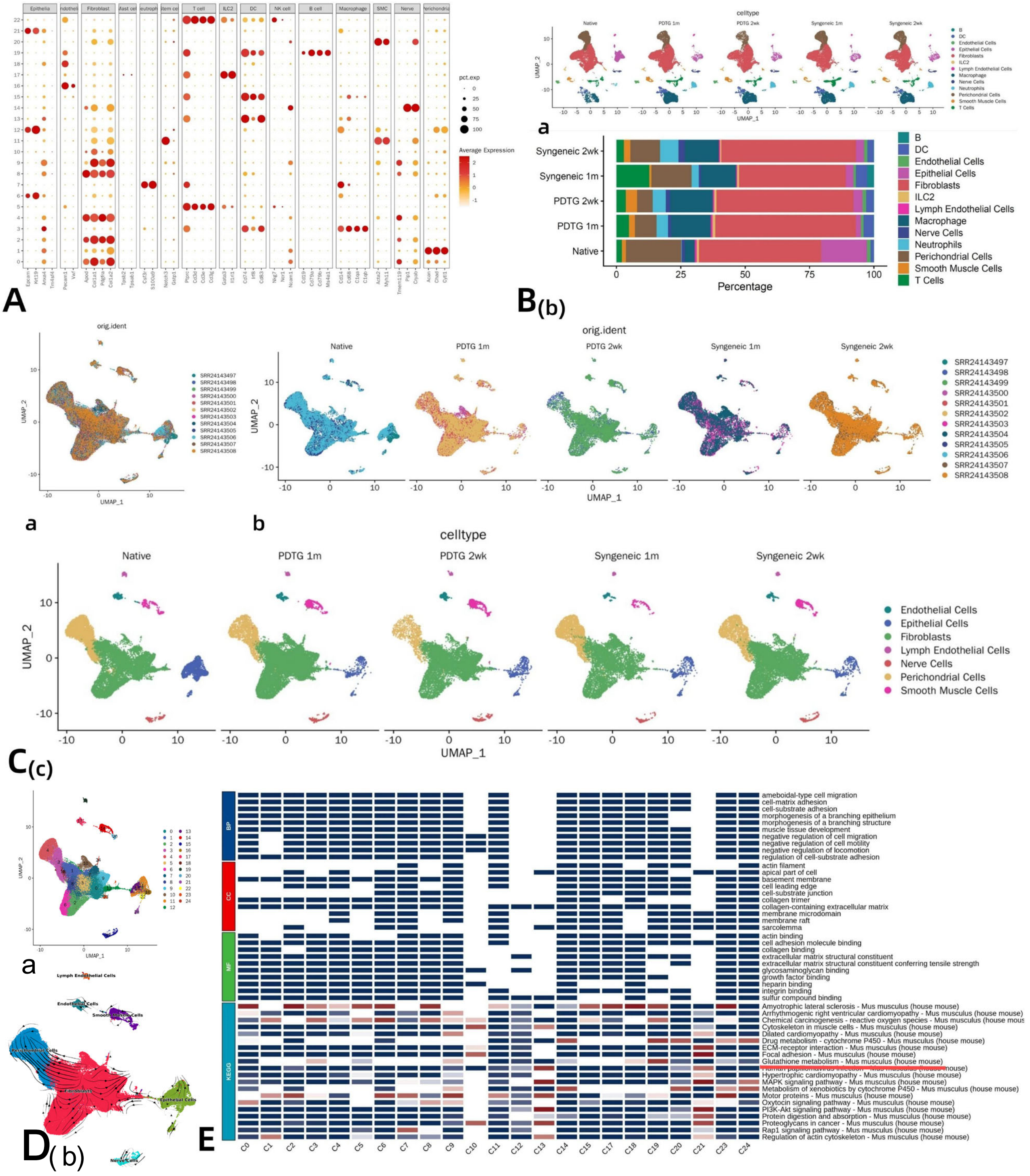

Fig. 3 | Single-cell RNA-seq analysis and pathway activation. A Dot plot illustrating the average expression and percentage of key markers across identified cell types, including endothelial cells, epithelial cells, fibroblasts, lymph endothelial cells, macrophages, nerve cells, perichondrial cells, smooth muscle cells, and T cells. The markers are categorized across different samples, with the color and size of dots reflecting the expression level and percentage, respectively; **B** UMAP plots (**a** and **b**) demonstrating cellular clustering based on their transcriptomic profiles at different time points and conditions (Native, PDTG 2 weeks, PDTG 1 month, Syngeneic 2 weeks, and Syngeneic 1 month). **Ba** shows the distribution of cells in terms of sample type, while **Bb** identifies specific cell types across these conditions. **C** Batch-corrected UMAP visualization across experimental groups (Native, PDTG 2 weeks, PDTG 1 month, Syngeneic 2 weeks, and Syngeneic 1 month). These visualizations confirm consistency in data integration while illustrating the distribution of cell types; **Da** Trajectory analysis demonstrating the differentiation pathways of progenitor cells, with emphasis on their progression towards specific lineages such as epithelial, chondrogenic, or fibroblastic pathways. **Db** Distinct branches in the trajectory map highlight major differentiation trajectories critical for graft regeneration; **E** Heatmap showcasing enriched gene ontology pathways among cell clusters. Pathways linked to cellular repair, extracellular matrix remodeling, and structural development are prominently displayed. The glutathione pathway has been specifically circled to highlight its significance, emphasizing its role in cellular redox homeostasis and tissue repair.

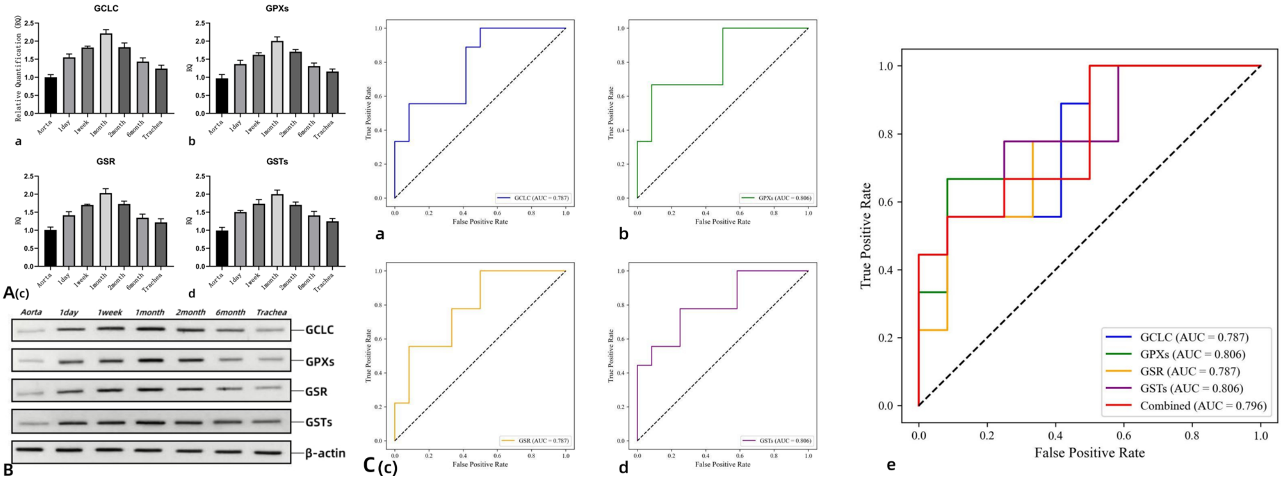

Fig. 4 | Validation of the glutathione pathway. A PCR results quantifying the mRNA levels of glutathione pathway enzymes at multiple postoperative intervals, showing elevated expressions compared to controls (**a**–**d**); **B** Western blot analysis of the protein expression levels of GCLC, GPXs, GSR, and GSTs, correlating with histological findings of tissue regeneration and oxidative stress response; **C** ROC curve analysis for individual enzymes and combined evaluation: **a** GCLC (AUC = 0.787), **b** GPXs (AUC = 0.806), **c** GSR (AUC = 0.787), **d** GSTs (AUC = 0.806), and **e** combined analysis (AUC = 0.796).

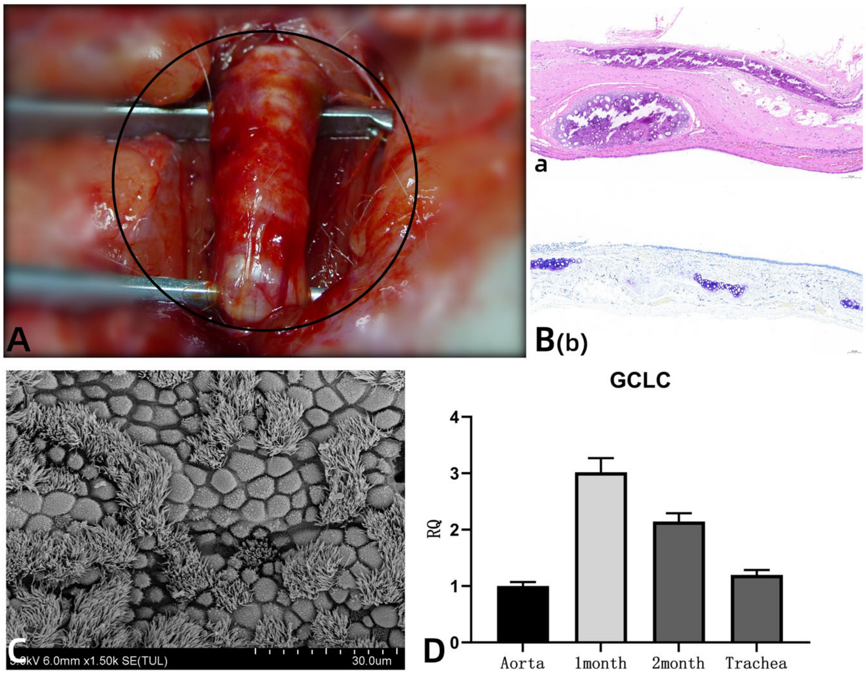

Fig. 5 | Effects of GCLC activation on tissue regeneration. A Histological comparison of grafts treated with α-lipoic acid showing accelerated cartilage development and complete structural maturation by the 3rd-month post-operation; **B** Further histopathological evaluations showing the formation of cartilage islands and ring-shaped formations earlier than in control groups (**Ba, b**); **C** SEM images detailing structural advancements at two months post-operation, akin to findings typically seen at three months in untreated models; **D** PCR analysis of GCLC expression levels was performed on samples from the treated group ($n = 6$ per time point) and control group ($n = 6$ per time point), as well as native aorta and tracheal tissues. The results highlight significantly elevated mRNA levels in treated grafts compared to controls and native tissues. **D** includes data from control animals, which serve as a baseline for comparison. The control group showed lower GCLC expression levels compared to the treated group, confirming the efficacy of α-lipoic acid in upregulating antioxidant defenses.

the importance of glutathione pathway activation during critical phases of oxidative stress management and tissue regeneration.

Enhanced tissue regeneration via GCLC activation

To investigate the effect of the glutathione pathway enzyme GCLC on tissue regeneration, an experimental regimen using α-lipoic acid, a GCLC agonist, was employed. Starting with 50 mg/kg daily for the first week and transitioning to 25 mg/kg three times weekly until the third month, this regimen aimed to enhance enzymatic activity during early graft healing.

Histological and imaging analyses demonstrated accelerated tissue regeneration, with treated grafts forming complete cartilaginous rings by the 3rd month—a process typically taking 6 months in controls (Fig. 5A). Histopathological examinations at two months revealed well-defined cartilage formations earlier than usual (Fig. 5Ba), and Toluidine Blue staining at one month highlighted early cartilage island formation (Fig. 5Bb).

Scanning Electron Microscopy at two months showed advanced structural developments (Fig. 5C). PCR analysis indicated that GCLC expression in treated grafts was significantly higher than in controls, peaking at 2.5-fold at one month and maintaining a 2.8-fold increase at two months post-operation (Fig. 5D). These results confirm the effectiveness of GCLC activation in promoting rapid and robust tissue regeneration.

Discussion

The adoption of aortic allografts in tracheal reconstruction represents a transformative approach in regenerative medicine, leveraging the structural and biomechanical properties inherent to these tissues[10]. The integration of these allografts, as demonstrated in our research, supports not only immediate structural needs but also encourages long-term functional restoration, as evidenced by the sustained cartilage development and minimal airway narrowing observed over time. This observation aligns with previous findings, which underscore the potential of aortic allografts to mimic native tracheal properties effectively, thus providing a conducive framework for tracheal regeneration[11–13].

Furthermore, the application of advanced imaging and stem cell tracking techniques has provided deeper insights into the cellular dynamics at play during the regeneration process. The significant increase in activated stem cells, particularly during the early postoperative phase, highlights their crucial role in tissue repair and regeneration. This increase aligns with theories positing that robust cellular proliferation is essential for successful graft integration and functional recovery, a concept supported by recent advancements in stem cell research which emphasize the importance of timely and effective stem cell engagement in regenerative processes[14].

The role of the glutathione pathway in cellular defense against oxidative stress, particularly in environments compromised by surgical trauma and ischemia, has been substantiated through the upregulation of key enzymes such as GCLC, GPXs, GSR, and GSTs during the early phases of graft healing[14]. Our study extends the understanding of this pathway, linking the heightened enzymatic response to improved regenerative outcomes, a connection that has been previously suggested but not empirically validated in the context of tracheal reconstruction. This enzymatic activity underscores the necessity of a robust antioxidant system for enhancing cellular survival and promoting effective integration of transplanted tissues[7].

The glutathione pathway plays a pivotal role in maintaining cellular redox homeostasis, which is important in the context of tracheal reconstruction, where oxidative stress can significantly impair healing and tissue integration. Our results, highlighting the elevated expression of key enzymes such as GCLC, GPXs, GSR, and GSTs, suggest activation of this antioxidant system in response to surgical trauma and subsequent ischemic conditions. This upregulation is likely a cellular defense mechanism against the elevated reactive oxygen species (ROS) generated during the surgical procedure and early recovery phases[15].

GCLC, the rate-limiting enzyme in glutathione synthesis, emerges as a critical player in this scenario. Its upregulation ensures an increased supply of glutathione, the main intracellular antioxidant, which directly neutralizes ROS and thereby mitigates cellular damage and supports survival pathways. The significant correlation between GCLC activation and accelerated cartilage regeneration in our models provides empirical support for its central role. This enzymatic activity not only protects cells from oxidative damage but also likely facilitates the cellular processes necessary for effective tissue repair and regeneration, such as cell proliferation, differentiation, and matrix deposition[6]. Further dissecting the role of GCLC within the glutathione pathway reveals its potential to influence other cellular functions crucial for tissue regeneration. For instance, glutathione is known to modulate inflammatory responses, a critical aspect of early healing phases. By regulating the redox-sensitive transcription factors that control the expression of pro-inflammatory cytokines, glutathione can help create a conducive environment for tissue repair and regeneration. Additionally, the antioxidant properties of glutathione may protect chondrocytes and other cellular constituents involved in cartilage formation, enhancing their viability and functionality during the critical phases of tracheal reconstruction[16].

Our study's focus on the glutathione pathway and GCLC has revealed significant insights into the biochemical and cellular dynamics essential for effective tissue regeneration. These findings illuminate the potential for targeting this pathway to improve regenerative outcomes. The versatility of the glutathione pathway suggests its applicability across various regenerative medicine and tissue engineering contexts. Future research should investigate how different pharmacological agents can modulate this pathway, aiming to enhance tissue healing and functional recovery in diverse clinical applications.

While the structural and histological analyses presented in this study provide strong evidence for the integration and maturation of the aortic allografts, direct functional assessments, such as airflow dynamics, mechanical stress testing, or in vivo functional studies, were not conducted. As such, conclusions regarding functional restoration are inferred based on structural findings and should be interpreted with caution. Future studies incorporating these direct measures will be essential to validate the functional capabilities of the grafts in clinical applications.

This study confirms the efficacy of aortic allografts for tracheal reconstruction, successfully mimicking native tracheal functions structurally and biomechanically. We showcased the crucial role of the glutathione pathway and related enzymes—GCLC, GPXs, GSR, and GSTs—in mitigating oxidative stress and bolstering cellular resilience during graft integration. Advanced imaging and histology provided deep insights into cellular dynamics, emphasizing the importance of activated stem cells in early postoperative recovery for successful tissue repair. Our research not only deepens our understanding of key cellular and biochemical processes vital for effective tracheal reconstruction but also suggests potential targeted therapies to enhance regenerative outcomes.

Data availability

The datasets used and/or analyzed during the current study can be obtained in Supplementary data.

Abbreviations

ROS	reactive oxygen species
GCLC	glutamate-cysteine ligase
GPXs	glutathione peroxidases
GSR	glutathione reductase
GSTs	glutathione S-transferases
IACUC	The Institutional Animal Care and Use Committee
H&E	hematoxylin and eosin
SEM	scanning electron microscope
TEM	transmission electron microscope
AFM	atomic force microscopy
PDTG	partially decellularized tracheal grafts
PCR	polymerase chain reaction

Received: 12 October 2024; Accepted: 14 February 2025;

References

1. Martinod, E. et al. Airway replacement using stented aortic matrices: long-term follow-up and results of the TRITON-01 study in 35 adult patients. *Am. J. Transpl.* **22**, 2961–2970 (2022).
2. Thierry, B., Arakelian, L., Denoyelle, F., Larghero, J. & Wurtz, A. Full circumferential human tracheal replacement: a systematic review. *Eur. J. Cardiothorac. Surg.* **66**, ezae269 (2024).
3. Seguin, A. et al. Tracheal regeneration: evidence of bone marrow mesenchymal stem cell involvement. *J. Thorac. Cardiovasc Surg.* **145**, 1297–1304.e2 (2013).
4. Han, Y., Lan, N., Pang, C. & Tong, X. Bone marrow-derived mesenchymal stem cells enhance cryopreserved trachea allograft epithelium regeneration and vascular endothelial growth factor expression. *Transplantation* **92**, 620–626 (2011).
5. Soriano, L. et al. Development and clinical translation of tubular constructs for tracheal tissue engineering: a review. *Eur. Respir. Rev.* **30**, 210154 (2021).
6. Averill-Bates, D. A. The antioxidant glutathione. *Vitam. Horm.* **121**, 109–141 (2023).
7. Lapenna, D. Glutathione and glutathione-dependent enzymes: from biochemistry to gerontology and successful aging. *Ageing Res Rev.* **92**, 102066 (2023).
8. Wei, S. et al. Tissue-engineered tracheal implants: advancements, challenges, and clinical considerations. *Bioeng. Transl. Med* **9**, e10671 (2024).
9. National Research Council (US) Committee for the Update of the Guide for the Care and Use of Laboratory Animals. *Guide for the Care*

and Use of Laboratory Animals 8th edn (National Academies Press (US), Washington, DC, 2011).

10. Paillusson, W. et al. Surgical management of penetrating neck injuries: An update. Part 1 - pre-hospital management. *J. Visc. Surg.* **161**, 310–316 (2024).
11. Wei, S. et al. Feasibility of tracheal reconstruction using silicone-stented aortic allografts. *Eur. J. Cardiothorac. Surg.* **65**, ezae115 (2024).
12. Tan, Z. H. et al. Regeneration of tracheal neotissue in partially decellularized scaffolds. *NPJ Regen. Med.* **8**, 35 (2023).
13. Kishimoto, K. et al. Synchronized mesenchymal cell polarization and differentiation shape the formation of the murine trachea and esophagus. *Nat. Commun.* **9**, 2816 (2018).
14. Hecht, F., Zocchi, M., Alimohammadi, F. & Harris, I. S. Regulation of antioxidants in cancer. *Mol. Cell* **84**, 23–33 (2024).
15. Singh, N., Sherin, G. R. & Mugesh, G. Antioxidant and prooxidant nanozymes: from cellular redox regulation to next-generation therapeutics. *Angew. Chem. Int. Ed. Engl.* **62**, e202301232 (2023).
16. Martinier, I. et al. Tunable biomimetic materials elaborated by ice templating and self-assembly of collagen for tubular tissue engineering. *Biomater. Sci.* **12**, 3124–3140 (2024).

Acknowledgements

We thank Yaoyao Xu in the core facility of The First Hospital of Jilin University for BMSCs culture. 1. Natural Science Foundation of Jilin Province (YDZJ202301ZYTS456); 2. Medicine & Engineering & Informatics Fusion and Transformation Key Laboratory of Luzhou City (XGY202407). 3. National Natural Science Foundations of China (12104177). 4. The First Hospital of Jilin University Doctor of Excellence program (JDYY-DEP-2024074).

Author contributions

Conceptualization: S.X. Wei and G.Y. Lv. Data curation: S.X. Wei and K.X. Duan. Formal analysis: Y.Y. Zhang, Z. Chen, and Y. Zhi. Funding acquisition: S.X. Wei, Z. Chen, M.Q. Li, and G.Y. Lv. Investigation: Y. Zhi. Methodology: Y.Y. Zhang and Y. Zhi. Project administration: M.Q. Li and G.Y. Lv. Resources: S.X. Wei and G.Y. Lv. Software: S.X. Wei. Supervision: S.X. Wei. Validation: S.X. Wei. Visualization: S.X. Wei and Y.Y. Zhang. Writing—original draft: S.X. Wei and Y. Zhi. Writing—review and editing: M.Q. Li and G.Y. Lv.

Competing interests

This manuscript has been approved by all authors and has not been submitted to any other journal. All authors confirm that there are no potential competing interests.

Ethical approval

The First Hospital of Jilin University Animal Experimental Ethics Committee (No. 2023-0639, Approval Date: 2023-09-07).

Additional information

Supplementary information The online version contains supplementary material available at https://doi.org/10.1038/s42003-025-07741-5.

Correspondence and requests for materials should be addressed to Guoyue Lv.

Peer review information *Communications Biology* thanks Mehmet Furkan Şahin, Yaaziel Melgarejo-Ramírez and the other, anonymous, reviewer(s) for their contribution to the peer review of this work. Primary Handling Editors: Dr. Ken-ichiro Kamei and Dr. Ophelia Bu. A peer review file is available.